

Z. Phys. Chem. **219** (2005) 715–741
© by Oldenbourg Wissenschaftsverlag, München

Classical Trajectory and Statistical Adiabatic Channel Study of the Dynamics of Capture and Unimolecular Bond Fission. VII. Thermal Capture and Specific Rate Constants $k(E, J)$ for the Dissociation of Molecular Ions

By J. Troe^{1,*}, V. G. Ushakov², and A. A. Viggiano³

¹ Institute for Physical Chemistry, University of Göttingen, Tammannstrasse 6,
D-37077 Göttingen, Germany

² Institute of Problems of Chemical Physics, Russian Academy of Sciences,
142432 Chernogolovka, Russia

³ Air Force Research Laboratory, Space Vehicles Directorate, 29 Randolph Rd,
Hanscom AFB, MA 01731-3010, USA

Dedicated to Prof. Dr. Jürgen Wolfrum at the occasion of his 65th birthday

(Received February 11, 2005; accepted February 16, 2005)

Reaction Kinetics / Unimolecular Reactions / Ion Fragmentations

Specific rate constants, $k(E, J)$, and thermal capture rate constants, $k_{\text{cap}}(T)$, are determined by statistical adiabatic channel model/classical trajectory (SACM/CT) calculations for unimolecular dissociation and the reverse association reactions of representative polyatomic molecular ions. Simple short-range valence/long-range ion-induced dipole model potentials without reverse barriers have been employed, using the reactions $\text{C}_8\text{H}_{10}^+ \rightleftharpoons \text{C}_7\text{H}_7^+ + \text{CH}_3$ and $\text{C}_9\text{H}_{12}^+ \rightleftharpoons \text{C}_7\text{H}_7^+ + \text{C}_2\text{H}_5$ as illustrative examples. Simplified representations of $k(E)$ and $k_{\text{cap}}(T)$ from rigid activated complex Rice–Ramsperger–Kassel–Marcus (RRKM) theory are compared with the SACM/CT treatment and with experimental results. The Massey parameters of the transitional mode dynamics, for the systems considered, are smaller than unity such that their dynamics is nonadiabatic while the dynamics of the conserved modes is adiabatic. Because of the long-range/short-range switching character of the potential, simple rigid activated complex RRKM theory cannot be used without modifications. The effects of a shifting of the effective bottle-neck of the dynamics with increasing energy towards smaller interfragment distances in the present cases are amplified by a shift into a range of increasing anisotropy of the potential. As a consequence, the thermal capture rate constants markedly decrease with increasing temperature.

* Corresponding author. E-mail: shoff@gwdg.de

20060117 467

REPORT DOCUMENTATION PAGE

Form Approved
OMB No. 0704-01-0188

The public reporting burden for this collection of information is estimated to average 1 hour per response, including the time for reviewing instructions, searching existing data sources, gathering and maintaining the data needed, and completing and reviewing the collection of information. Send comments regarding this burden estimate or any other aspect of this collection of information, including suggestions for reducing the burden to Department of Defense, Washington Headquarters Services, Directorate for Information Operations and Reports (0704-0188), 1215 Jefferson Davis Highway, Suite 1204, Arlington VA 22202-4302. Respondents should be aware that notwithstanding any other provision of law, no person shall be subject to any penalty for failing to comply with a collection of information if it does not display a currently valid OMB control number.

PLEASE DO NOT RETURN YOUR FORM TO THE ABOVE ADDRESS.

1. REPORT DATE (DD-MM-YYYY) 16-02-2005		2. REPORT TYPE REPRINT		3. DATES COVERED (From - To)	
4. TITLE AND SUBTITLE Classical Trajectory and Statistical Adiabatic Channel Study of the Dynamics of Capture and Unimolecular Bond Fission. VII. Thermal Capture and Specific Rate Constants $k(E, J)$ for the Dissociation of Molecular Ions				5a. CONTRACT NUMBER	
				5b. GRANT NUMBER	
				5c. PROGRAM ELEMENT NUMBER 61102F	
6. AUTHORS J. Troe*, V.G. Ushakov**, and A.A. Viggiano				5d. PROJECT NUMBER 2303	
				5e. TASK NUMBER BM	
				5f. WORK UNIT NUMBER A1	
7. PERFORMING ORGANIZATION NAME(S) AND ADDRESS(ES) Air Force Research Laboratory /VSBXT 29 Randolph Road Hanscom AFB, MA 01731-3010				8. PERFORMING ORGANIZATION REPORT NUMBER AFRL-VS-HA-TR-2005-1190	
9. SPONSORING/MONITORING AGENCY NAME(S) AND ADDRESS(ES)				10. SPONSOR/MONITOR'S ACRONYM(S) AFRL/VSBXT	
				11. SPONSOR/MONITOR'S REPORT NUMBER(S)	
12. DISTRIBUTION/AVAILABILITY STATEMENT Approved for public release; distribution unlimited.					
13. SUPPLEMENTARY NOTES Reprinted from Z. Phys. Chem. V. 219 (2005), pp. 715-741. © Oldenbourg Wissenschaftsverlag, Munich, Germany. *University of Goettingen, Goettingen, Germany. **Inst. for Problems of Chem. Phys., Russian Acad. of Sciences, 142432 Chernogolovka, Russia					
14. ABSTRACT Specific rate constants $k(E, J)$ and thermal capture rate constants, $k_{cap}(T)$, are determined by statistical adiabatic channel model/classical trajectory (SACM/CT) calculations for unimolecular dissociation and the reverse association reactions of representative polyatomic molecular ions. Simple short-range valence/long-range ion-induced dipole model potentials without reverse barriers have been employed, using the reactions $C_8H_{10}^+ \rightleftharpoons C_7H_7^+ + CH_3$ and $C_9H_{12}^+ \rightleftharpoons C_7H_7^+ + C_2H_5$ as illustrative examples. Simplified representations of $k(E)$ and $k_{cap}(T)$ from rigid activated complex Rice-Ramsperger-Kassel-Marcus (RRKM) theory are compared with the SACM/CT treatment and with experimental results. The Massey parameters of the transitional mode dynamics, for the systems considered, are smaller than unity such that their dynamics is nonadiabatic while the dynamics of the conserved modes is adiabatic. Because of the long-range/short-range switching character of the potential, simple rigid activated complex RRKM theory cannot be used without modifications. The effects of shifting of the effective bottleneck of the dynamics with increasing energy towards smaller interfragment distances in the present cases are amplified by a shift into a range of increasing anisotropy of the potential. As a consequence, the thermal capture rate constants markedly decrease with increasing temperature.					
15. SUBJECT TERMS Classical trajectory Statistical adiabatic channel Bond fission Capture Reaction kinetics Unimolecular reactions Ions					
16. SECURITY CLASSIFICATION OF:			17. LIMITATION OF ABSTRACT	18. NUMBER OF PAGES	19a. NAME OF RESPONSIBLE PERSON
a. REPORT	b. ABSTRACT	c. THIS PAGE			A. A. Viggiano
UNCL	UNCL	UNCL	UNL		19b. TELEPHONE NUMBER (Include area code) (781) 377-4028

1. Introduction

In the previous articles of this series [1–6], we have treated unimolecular bond fission and the reverse association reactions by a combination of the statistical adiabatic channel model (SACM) and classical trajectory (CT) calculations. The dissociative separation of two species and the reverse associative capture process forming a bound adduct were followed, in reduced dimensionality, by explicitly treating the dynamics of the transitional modes (external rotations of the fragments) while conserved modes (internal modes of the fragments) were handled adiabatically. The SACM/CT approach is able to establish a direct link between the potential energy surfaces (PESs) and thermal rate constants for capture $k_{\text{cap}}(T)$ (or the corresponding high pressure rate constants for recombination and the reverse dissociation) such as demonstrated in [1–5]. In addition, specific rate constants $k(E, J)$ for unimolecular bond fissions as a function of the energy E and the angular momentum (quantum number J) can be derived in a way which is consistent with the thermal capture rate constants, see [6].

Calculating the J -dependence of $k(E, J)$ is an important element of the analysis, since thermal capture involves broad distributions over E and J . In addition, complex-forming bimolecular reactions, to which the same approach may be applied, involve subtle competitions between E - and J -dependent competing association and dissociation processes of the adducts [7]. Generally, the J -dependence is handled in a more simplified manner than presented here and the employed average J -treatments are not always adequate, see *e.g.* [8].

It is obvious that the kinetic properties are governed by PESs such that direct links between potentials and rate parameters need to be established in a transparent way. For this reason, we have calculated thermal capture rate constants [1–5] and the corresponding specific rate constants [6] for a series of interfragment potentials such as ion–dipole [1], ion–quadrupole [2], dipole–dipole [3], atom–linear rotor model valence [4], and linear rotor–linear rotor model valence [5] potentials. By using such model potentials, insight into what specifically controls the reactivity is developed. SACM- and CT-treatments of the transitional mode dynamics were shown to coincide in the limit of adiabatic and classical behavior. Nonadiabatic dynamics and quantum effects were also investigated. It was shown [9] that the SACM/CT concept works down to temperatures in the milli- and even micro-Kelvin range, particularly if Coriolis coupling effects are properly accounted for [10]. The presence of open electronic shells also becomes relevant at low temperatures and needs to be taken into account, see *e.g.* [11] and [12].

The transitional mode potentials considered in [1–6] were partly of “mixed” (ion–permanent plus induced dipole [1], ion–quadrupole plus induced dipole [2], dipole–dipole plus dispersion [3]), partly of “homogeneous” valence character [4, 5]. The former potentials [1–3] were characterized by regions of differing anisotropies while the latter [4, 5] had uniform anisotropies. This raises the question which parts and properties of the potential are most

relevant for the dynamics. Answers are provided by inspecting the positions of maxima of adiabatic channel potential curves in SACM [13] or positions of transition states in flexible variational transition state theory (VTST) [14]. With both approaches one observes a smooth “transition state shifting” towards smaller interfragment distances with increasing energy such that regions of different anisotropy characters may be sampled. There may also be more abrupt “transition state switching” if the PESs have small barriers or reefs along the reaction coordinate such as found in *ab initio* calculations of PESs for small molecules like HO_2 [15], HOCO [16], or H_2O_2 [17]. Whether transition state switching also occurs without barriers or reefs, remains an open question [8] and one would like to find an answer by SACM/CT calculations on the given PESs. However, there is a problem: if the transitional mode dynamics is nonadiabatic, adiabatic channel potential curves lose their significance and sampling of phase space volumes in simple VTST likewise loses its rigorous relation to dynamics. Even the most elaborate variable reaction coordinate VTST [18], requires “dynamical corrections” to be determined by CT calculations [19].

In the present work we consider PESs of mixed character, *i.e.* valence-ion-induced dipole potentials, which link regions of quite different anisotropies. For such potentials, a switching between inner tight and outer orbiting transition states has been invoked for molecular ions [20] when transitional mode frequencies along the reaction coordinate were assumed to change in a way which strongly differs from the changes of the minimum energy path (MEP) potential. The question remains [8, 20, 21] to what extent true transition state switching is a consequence of the chosen potential and of the general approach, and whether transition state switching is real for molecular ions besides the normal transition state shifting. Because of the general importance of this question we apply the SACM/CT approach to polyatomic ions with model PESs of the described mixed character. We focus attention on an internally consistent calculation of specific rate constants $k(E, J)$ and thermal capture rate constants, $k_{\text{cap}}(T)$. In a separate publication [22], we also provide an SACM/CT calculation of product energy distributions (PEDs) which are internally consistent with the present calculations. Our results for $k(E, J)$, $k_{\text{cap}}(T)$ and PEDs show all signs of a transition state shifting or transition state switching but cannot distinguish between them. With increasing E , J , or T , dynamical constraints caused by the increasing anisotropy of the PES at shorter interfragment distances lead to results which would correspond to increasingly rigid transition states. Since the chosen reaction systems show nonadiabatic transitional mode dynamics, however, for principal reasons it would be difficult if not impossible to rigorously define transition states. Since there is also no real need to look for them, the question of transition state shifting or switching finally becomes irrelevant. Previous transition state switching treatments [20] have not provided such a consistent approach as the full J -dependence was not elaborated.

The outline of the present article is as follows. First, we construct reduced dimensionality model PESs for transitional modes in molecular ion dissociations. We use the dissociations of alkylbenzene ions as practical examples because conventional modelling of $k(E)$ for these systems by rigid activated complex Rice–Ramsperger–Kassel–Marcus (RRKM) theory and experimental results are available. Classical trajectory calculations are performed on these PESs, leading to $k(E, J)$ and $k_{\text{cap}}(T)$ (and PEDs(E, J), see [22]). A minimum of fitting of the potentials is necessary to bring modelled $k(E, J)$ into agreement with the experiments. The corresponding rate constants $k_{\text{cap}}(T)$ then are obtained by thermal averaging of $k(E, J)$ and again compared with experiments. Various fitting procedures of both the potential and the rate constants are inspected and compared with traditional RRKM modelling with the goal to identify the most economic, but still realistic treatment in practical applications, in particular with respect to the relation between specific and thermal rate constants.

2. Model potentials for the dissociation of polyatomic molecular ions

The SACM/CT approach treats the dynamics of the transitional modes explicitly such that an analytical, reduced dimensionality, PES in these coordinates is required. The potential of the conserved modes is simplified assuming that these mostly vibrational modes are adiabatic and that their frequencies are close to the fragment frequencies. The latter approximation could be relaxed by correcting for the change of the frequencies along the interfragment distance and choosing frequencies, *e.g.*, near to the positions of the centrifugal barriers.

The SACM/CT method calculates trajectories in the transitional mode potential. Initial conditions for these CT calculations are two fragments at large separation. Combining their individual rotational angular momenta into one total angular momentum, the number $W_0(E, J)$ of their quantum states of total energy E and total angular momentum (quantum number J) is calculated first. During the approach of the two fragments, “capture” occurs when the inner turning point of the relative motion is clearly inside the well of the bound adduct.

Neglecting the anisotropy of the potential, a capture probability $w^{\text{PST}}(E, J)$ then is defined which denotes that fraction of the $W_0(E, J)$ quantum states which lead to capture in the artificially isotropic potential. In general, the product $W^{\text{PST}}(E, J) = w^{\text{PST}}(E, J)W_0(E, J)$ will be smaller than $W_0(E, J)$ because dynamical constraints arise in the form of centrifugal barriers, $E_0(J)$. $W^{\text{PST}}(E, J)$ is termed the “number of open channels” (or of “activated complex states”) in phase space theory (PST). One should note that our version of PST differs from other versions of PST [8, 23], *e.g.* from the simplest form in which centrifugal barriers are completely neglected. Our version of PST also differs

from orbiting transition state PST (OTS/PST) where centrifugal barriers $E_0(J)$ are calculated with the long-range electrostatic potential only [24]. The present PST provides a rigorous upper limit of the capture rate which would not be the case in OTS/PST which neglects short-range components of the PES, see below.

Including the anisotropy of the real potential introduces additional dynamical constraints such that the product of the corresponding capture probability $w(E, J)$ and $W_0(E, J)$, *i.e.* $W(E, J) = w(E, J)W_0(E, J)$, is smaller than $W^{\text{PST}}(E, J)$. Convoluting the numbers of open channels $W(E, J)$ of the transitional modes with the contributions of conserved modes completes the calculation of the total number of open channels $W_{\text{tot}}(E, J)$. Thermal averages over $W_{\text{tot}}(E, J)$ determine the thermal capture rate constants, $k_{\text{cap}}(T)$. At the same time, $W_{\text{tot}}(E, J)$ also enters the expression for specific rate constants $k(E, J) = W_{\text{tot}}(E, J)/h\rho(E, J)$ such as employed in statistical unimolecular rate theory [8]. $\rho(E, J)$ in the usual way denotes the rovibrational density of states.

SACM/CT calculations in the past have been performed on *ab initio* potentials, see *e.g.* [15] and [17], and on model potentials, see [4] and [5]. In the present work, we are interested in polyatomic ions for which *ab initio* potentials are available only in rare cases (see, *e.g.*, [25–27]). For this reason, we design simple model potentials which connect short-range valence with long-range electrostatic potentials. The transition between the two components of the PES can be smooth like calculated for LiH_2^+ dissociation [26] or abrupt like derived for C_6H_6^+ dissociation [25]. Unfortunately, often *ab initio* calculations of PESs for molecular ions (like the PES for N_4^+ dissociation from [27]) are not extended to that range of interfragment distances where the transition from short-range to long-range potential occurs such that there is no *a priori* guide to the design of the model potential. For the $\text{C}_8\text{H}_{10}^+$ and $\text{C}_9\text{H}_{12}^+$ -systems of primary interest in the present article, we decided to construct a model potential with smooth short-range/long-range switching. Because of the model character of the potential, we had to allow for the introduction of one fitting parameter which was chosen to be an anisotropy amplitude factor. However, this fitting parameter was fixed by means of a single measurement and no more fitting was allowed for comparison with other measurements.

2.1 Radial part of the potential

It is important to realize which property of the rate constants is governed by the radial part of the potential and which is connected to the anisotropy. For this reason, we first consider the radial part of our model potential only. The short-range component of this potential is assumed to be of Morse type

$$V^{\text{SR}}(r) = D\{\exp[-2\beta(r-r_e)] - 2\exp[-\beta(r-r_e)]\}. \quad (2.1)$$

In the present work we consider a long-range induced-dipole component of the potential of the form

$$V^{\text{LR}}(r) = -\alpha q^2 / 2r^4 \quad (2.2)$$

(for our nomenclature see [1–6]), but other long-range potentials could be treated in an analogous way. Including the ion-dipole term has little effect on the present calculations since the polarizability is large and the dipole moment is small. We assume that the center-of-mass (c.o.m.) distance r between the fragments can serve as the reaction coordinate and that the radial potential $V(r)$ is the MEP potential.

There are various ways to represent the switching of $V(r)$ between $V^{\text{SR}}(r)$ and $V^{\text{LR}}(r)$. For example, one may try to use an expression [26]

$$V(r) \approx V^{\text{SR}}(r)F(r) + V^{\text{LR}}(r)[1 - F(r)] \quad (2.3)$$

where $F(r)$ is an exponentially decaying switching function. In the present work a more sophisticated switching procedure was employed for reasons which become clear below. We modified $V^{\text{LR}}(r)$ in two stages. First, Eq. (2.2) was replaced by

$$V^{\text{LR}}(r) = -\alpha q^2 / 2r_{\text{B}}^4 \quad (2.4)$$

where r_{B} , instead of the c.o.m. distance r , denotes the length of the breaking (or of the forming) bond. We then removed the discontinuity of the denominator of Eq. (2.4) by adding a term $\alpha q^2 / 2D$, such that

$$V^{\text{LR}}(r) \approx -\frac{\alpha q^2 / 2}{(r - \Delta r_{\text{B}})^4 + \alpha q^2 / 2D} \quad (2.5)$$

where $\Delta r_{\text{B}} = r_{\text{e}} - r_{\text{Be}}$ (the subscript e denotes equilibrium values of r and r_{B}). Second, instead of an exponential switching function, we used

$$V(r) = V^{\text{SR}}(r)[1 - \kappa F] + V^{\text{LR}}(r)F \quad (2.6)$$

with $V^{\text{SR}}(r)$ from Eq. (2.1), and $V^{\text{LR}}(r)$ from Eq. (2.5). F and κ are defined as

$$F = 1 / \{1 + \exp[-2\beta(r - r_{\text{sw}})]\}, \quad (2.7)$$

and

$$\kappa = 1 - \frac{\alpha q^2}{4D(r_{\text{sw}} - \Delta r_{\text{B}})^4}. \quad (2.8)$$

r_{sw} denotes that value of r where $V^{\text{LR}}(r)$ from Eq. (2.5) intersects with $V^{\text{SR}}(r)$ from Eq. (2.1). The radial MEP potential from Eqs. (2.6)–(2.8) was designed to produce a smooth monotonic transition from Eq. (2.1) to Eq. (2.2).

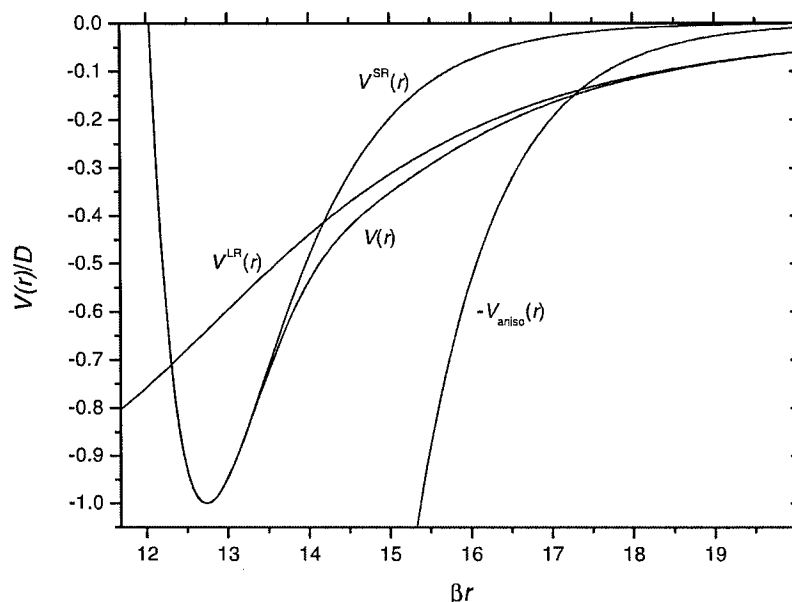


Fig. 1. Radial potential $V(r)$ for the reaction $\text{C}_8\text{H}_{10}^+ \rightleftharpoons \text{C}_7\text{H}_7^+ + \text{CH}_3$ (short-range Morse potential $V^{\text{SR}}(r)$ from Eq. (2.1); modified long-range ion-induced dipole potential $V^{\text{LR}}(r)$ from Eq. (2.5); model potential $V(r)$ from Eqs. (2.6)–(2.8); maximum angular potential $V_{\text{aniso}}(r) = C_1 \exp[-\beta(r - r_e)]$ with $C_1/D \approx 14$ from Eq. (2.15) for ion-dipole type anisotropy; for molecular parameters, see Appendix, all quantities represented as $V(r)/D$).

In order to achieve the smooth transition for various systems, the expression for κ needed some flexibility; e.g. Eq. (2.8) was found to be adequate for the reaction $\text{C}_8\text{H}_{10}^+ \rightarrow \text{C}_7\text{H}_7^+ + \text{CH}_3$, whereas Eq. (2.9) was preferred for $\text{C}_9\text{H}_{12}^+ \rightarrow \text{C}_7\text{H}_7^+ + \text{C}_2\text{H}_5$,

$$\kappa = 1 - \frac{\alpha q^2}{D (r_{\text{SW}} - \Delta r_{\text{B}})^4} \quad (2.9)$$

because it gave a smoother transition than Eq. (2.8). We illustrate the modelled MEP potentials for the dissociations of $\text{C}_8\text{H}_{10}^+$ and $\text{C}_9\text{H}_{12}^+$ in Figs. 1 and 2. We use the molecular parameters specified in Appendix A. The modelled MEP potential shows smooth, but relatively fast, transitions between $V^{\text{SR}}(r)$ from Eq. (2.1) and $V^{\text{LR}}(r)$ from Eq. (2.5). It gives major deviations from the short-range valence potential above about $V(r)/D \approx -0.5$, similar to the *ab initio* PES for the $\text{LiH}_2^+ \rightarrow \text{Li}^+ + \text{H}_2$ reaction [26] which shows major deviations from a Morse-type valence potential at $V(r)/D$ above about -0.5 . However, in the case of the production of an atomic ion, the long-range potential at $V(r)/D \approx -0.5$ does not intersect, but only comes close to the short-range potential. For the considered polyatomic ions, long-range potentials from Eq. (2.2) would

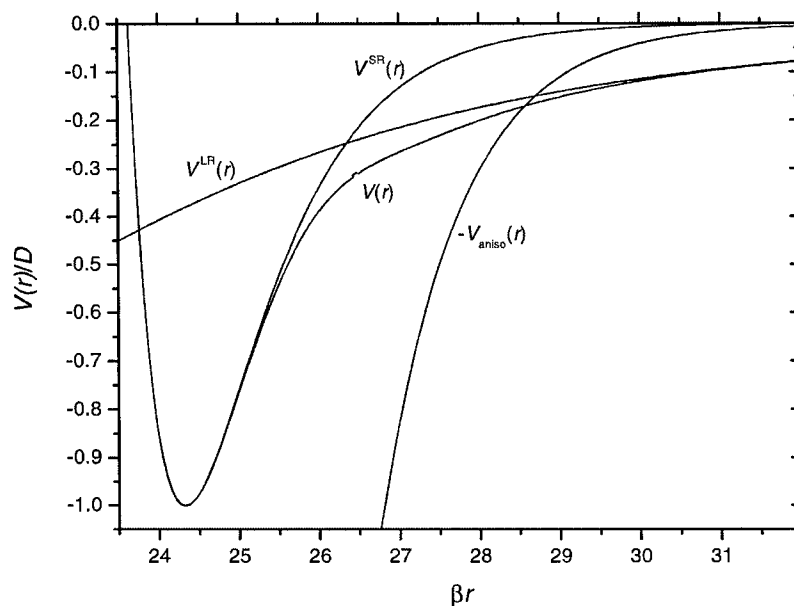


Fig. 2. As Fig. 1, for $\text{C}_9\text{H}_{12}^+ \rightleftharpoons \text{C}_7\text{H}_7^+ + \text{C}_2\text{H}_5$ (with $C_1/D \approx 12$).

intersect the short-range potential at $V(r)/D$ above about -0.05 . For this reason, replacing r by r_B in Eq. (2.2) appears more physical, leading to the results shown in Figs. 1 and 2.

The radial potentials are all that is required for a PST calculation of $W(E, J)$. In particular, one may directly determine the centrifugal barriers $E_0(J)$, i.e. the maxima of the centrifugal potentials $V(r) + L(L+1)\hbar^2/2\mu r^2$ (L = quantum number of orbital angular momentum). In the present case, one may apply the simplification $J \approx L$, see below. For the $\text{C}_8\text{H}_{10}^+$ system, one obtains

$$E_0(J)/hc \approx 3.18 \times 10^{-6} \text{ cm}^{-1} [J^4 / (1 + 0.0169J + 2.65 \times 10^{-4} J^{1.79})]. \quad (2.10)$$

The corresponding expression for the $\text{C}_9\text{H}_{12}^+$ system is $E_0(J)/hc \approx 5.90 \times 10^{-7} \text{ cm}^{-1} [J^4 / (1 + 9.73 \times 10^{-3} J^{1.075} + 5.21 \times 10^{-6} J^{2.166})]$. For small J , in both cases $E_0(J)$ of the ion-induced dipole potential is approached, such as given by

$$E_0(J) = [J(J+1)\hbar^2/2\mu]^2 / 2\alpha q^2. \quad (2.11)$$

For large J , $E_0(J)$ takes the form typical for Morse valence potentials [28], i.e.

$$E_0(J) \approx C_v [J(J+1)]^v \quad (2.12)$$

with ν being in the range 1 to 1.5. Eq. (2.10) shows a smooth transition between Eqs. (2.11) and (2.12) for the $\text{C}_8\text{H}_{10}^+$ and $\text{C}_9\text{H}_{12}^+$ systems. For the model potentials of the present work, there is no sign of centrifugal barrier switching such as found for potentials with small barriers or reefs, see e.g. the $\text{H}_2\text{O}_2 \rightarrow 2\text{OH}$ reaction [17].

Centrifugal pseudo-partition functions

$$Q_{\text{cent}} = \sum_{J=0}^{\infty} (2J+1) \exp[-E_0(J)/kT] \quad (2.13)$$

with Eq. (2.10) are easily calculated and capture rate constants in PST are accessible through

$$k_{\text{cap}}^{\text{PST}} = \frac{kT}{h} \left(\frac{h^2}{2\pi\mu kT} \right)^{3/2} Q_{\text{cent}} \quad (2.14)$$

A special case of Eq. (2.14) would be ion-induced dipole capture, for which Eqs. (2.11)–(2.13), and (2.14) give the Langevin rate constant $k_L = 2\pi q(\alpha/\mu)^{1/2}$. OTS/PST and the present version of PST in this special case coincide and lead to the same result of $k_{\text{vsp}}^{\text{PST}} = k_L$.

2.2 Angular part of the potential

While the here considered long-range ion-induced dipole potential is isotropic, the short-range valence potential is always strongly anisotropic. As a consequence of this anisotropy, the free rotations of the separated fragments change into deformation vibrations of the adduct. The rapidity of this change is related to the particular character of the PES, *i.e.* either a smooth or an abrupt switching from the short-range to the long-range component of the potential. As discussed above, we here decided to assume a smooth switching. However, we are aware of the fact that also more abrupt switchings like in C_6H_6^+ dissociation [25] are possible.

We modelled the anisotropy of the PES by angular terms like

$$V(r, \text{angles}) \approx V(r) + C_1 \exp[-\beta(r - r_e)] \{ (2 + \mathbf{d}_1 \mathbf{n} + \mathbf{d}_2 \mathbf{n}) / 4 \} \quad (2.15)$$

for an anisotropy of ion-dipole type (\mathbf{d}_1 and \mathbf{d}_2 are unit vectors along the axis of the fragment rotors and \mathbf{n} is the unit vector in the direction of the breaking bond; C_1 characterizes the strength of the anisotropy; one should note that in a true ion-dipole system \mathbf{n} would be in the direction of the line connecting the c.o.m.s). Alternatively, we considered

$$V(r, \text{angles}) \approx V(r) + C_2 \exp[-\beta(r - r_e)] \{ [2 + \mathbf{d}_1 \mathbf{d}_2 - 3(\mathbf{d}_1 \mathbf{n})(\mathbf{d}_2 \mathbf{n})] / 4 \} \quad (2.16)$$

for an anisotropy of dipole–dipole type (\mathbf{d}_1 and \mathbf{d}_2 are unit vectors like in Eq. (2.15), \mathbf{n} is the unit vector in the direction of the line connecting the c.o.m.s; C_2 characterizes the strength of the anisotropy). Figs. 1 and 2 include amplitudes of the anisotropy such as described by initially arbitrarily chosen values of C_1 . Quite similar to the example [26] of LiH_2^+ , our model PESs show anisotropies which reach far beyond the range of the short-range valence potential into the range of the long-range ion-induced dipole potential.

Performing CT calculations on the model potentials, we realized that the angular form (ion–dipole or dipole–dipole character) is only of secondary importance. What matters is the anisotropy amplitude represented by the values of the amplitude factors C_1 or C_2 . This quantity needs to be fitted such as discussed below. In addition, Eqs. (2.15) and (2.16) only model anisotropies of linear rotor fragments leading to a linear rotor adduct. In reality, there will be additional anisotropy corresponding to the top character of the fragments. In the absence of more information on this property of the PES, we limited ourselves to studying the dynamics with potentials given by Eqs. (2.15) or (2.16).

3. Capture probabilities and numbers of open channels

Before performing CT calculations of the transitional mode dynamics on the model potentials described in Sect. 2, it appeared useful to analyze the character of the dynamics with respect to the effective mass M and the corresponding Massey parameter $\xi = (2M)^{1/2}$, see [6]. The Massey parameter corresponds to the ratio between the collision time in the radial potential $V(r)$ and the period of motion of the considered mode. If $\xi \gg 1$, the motion of the mode stays adiabatically in its quantum states which can be calculated by solving the eigenvalue problem for fixed interfragment distances. This leads to the adiabatic channel potential curves of SACM [13]. If $\xi \ll 1$, these curves lose their significance, there are frequent transitions between the adiabatic channel potential curves, and the dynamics for $\xi \rightarrow 0$ approaches the “sudden” limit. Conserved modes generally are on the adiabatic side while transitional modes may be more or less nonadiabatic. This is the reason why SACM/CT concepts [1–6] have been developed by us beyond the original SACM model [13].

In the case of an isotropic potential, adiabatic ($\xi \gg 1$) and sudden ($\xi \ll 1$) dynamics of transitional modes lead to identical capture rates. It is the anisotropy of the potential which generates marked differences between adiabatic and sudden dynamics such as illustrated in [1] for ion–dipole capture and in [4] and [5] for valence potentials. The Massey parameters for a valence potential are independent of the energy and are given by

$$\xi \approx (2\mu B)^{1/2} / \hbar\beta \quad (3.1)$$

with the reduced mass μ , the Morse parameter β , and $B = (B_1 + B_2)/2$ where B_1 and B_2 are the relevant rotational constants of the two fragments (in energy

units). Based on the molecular parameters of Appendix A, we find the following quantities for $\text{C}_8\text{H}_{10}^+$: $B_1/hc \approx 0.078 \text{ cm}^{-1}$ and $B_2/hc \approx 9.3 \text{ cm}^{-1}$ which leads to $\xi = (2M)^{1/2} \approx 0.51$. Separating the contributions of the rotors would give $\xi_1 \approx 0.066$ and $\xi_2 \approx 0.72$. For $\text{C}_9\text{H}_{12}^+$ with $B_2/hc \approx 0.73 \text{ cm}^{-1}$, we obtain $\xi_1 \approx 0.066$, $\xi_2 \approx 0.20$, and $\xi \approx 0.15$. The larger rotational constants of CH_3 compared to C_2H_5 are the reason for larger ξ_2 and ξ in $\text{C}_8\text{H}_{10}^+$ compared to $\text{C}_9\text{H}_{12}^+$. In spite of the fact that these estimates are only approximate, it is clear that ξ_1 , ξ_2 , and ξ are below unity. Therefore, for the molecular ions considered here, there will be marked deviations in the dynamics from the adiabatic limit (reductions of k_{cap} up to about 40%, see [1], [4], and [5]).

Details of our CT calculations have been described previously [1–6] and are not repeated here. The initial conditions of the trajectories were selected randomly from a uniform phase space distribution compatible with the respective E and J . About 10^4 trajectories were required to reduce statistical scatter of the results for a given (E, J) to less than 2%. Thermal capture rates were determined either by thermal averaging of the (E, J) -results or by thermally weighted selection of initial conditions [1]. Both methods gave identical results, confirming the validity of the numerical procedure.

Our determination of the number of open channels $W(E, J)$ for the transitional modes starts from the well known state-counting for free rotor-pairs of joint total E and J^{28-30} . In the absence of centrifugal barriers this defines $W_0(E, J)$. The result for large J is

$$W_0(E, \text{large } J) = \pi E^3 / 6\sigma_1\sigma_2 \prod_{i=1}^3 B_{1i}^{1/2} B_{2i}^{1/2} \quad (3.2)$$

where B_{1i} and B_{2i} are the rotational constants (in energy units) and σ_1 and σ_2 the symmetry numbers of fragments 1 and 2, respectively. For small J , treating the fragments as spherical tops (with rotational constants B_1 and B_2), one has

$$W_0(E, \text{small } J) \approx 8(2J+1)E^{5/2} / 15\sigma_1\sigma_2 B_1 B_2 (B_1 + B_2)^{1/2}. \quad (3.3)$$

State-counting for asymmetric top fragments is also easily done. In practice, an empirical interpolation between Eqs. (3.2) and (3.3), such as described in [28], often suffices: with $y = W_0(E, J)/W_0(E, \text{large } J)$ and $x = W_0(E, \text{small } J)/W_0(E, \text{large } J)$, one may use

$$y \approx \{0.08x^{1/2} \exp[-1.1(x-1)^2] + 1\} \tanh x. \quad (3.4)$$

An alternative interpolation between Eqs. (3.2) and (3.3) using $\text{erf}(x)$ was proposed in [31].

The appearance of centrifugal barriers $E_0(J)$ on the MEP potential, such as given by Eqs. (2.10)–(2.12), leads to the PST expression

$$W^{\text{PST}}(E, J) = w^{\text{PST}}(E, J) W_0(E, J). \quad (3.5)$$

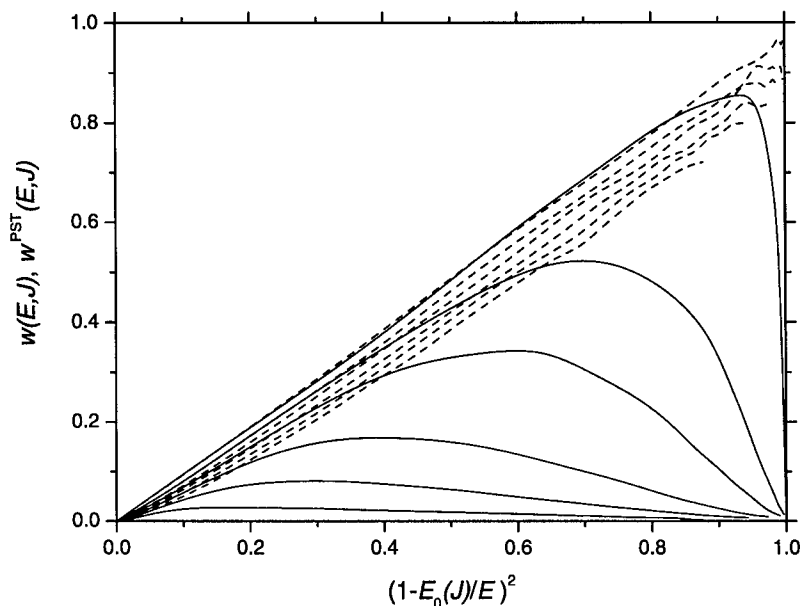


Fig. 3. Capture probabilities for an isotropic potential (PST) and an anisotropic potential $w^{\text{PST}}(E, J)$ (dashed) and $w(E, J)$ (full), respectively (from top to bottom curves for, $J = 25, 55, 75, 105, 135$, and 180 with $E_0(J)/hc = 0.83, 12.8, 35, 99.5, 211$, and 481 cm^{-1} , respectively; results for $\text{C}_8\text{H}_{10}^+$ with dipole-dipole type anisotropy with $C_2/D \approx 20$).

The capture probability $w^{\text{PST}}(E, J)$ was either determined by CT calculations on the radial potential of Sect. 2 or by state-counting with the condition $E \geq E_0(J)$. Figs. 3 and 4 include the results for the $\text{C}_8\text{H}_{10}^+$ system for the two choices of anisotropy used. Like in our earlier work [6], for two molecular fragments,

$$w^{\text{PST}}(E, J) \approx [1 - E_0(J)/E]^2 \quad (3.6)$$

provides an adequate approximation (for an atom and one molecular fragment, the exponent 2 in Eq. (3.6) would be replaced by unity; one should note that the centrifugal barriers E_0 depend on J as well as on the orbital angular momentum with quantum number L ; the results shown for $w^{\text{PST}}(E, J)$ in Figs. 3 and 4 are for randomly selected L and, therefore, are slightly scattered and somewhat below $[1 - E_0(J)/E]^2$).

While Eqs. (3.2)–(3.6) provide easy access to the PST results for $w^{\text{PST}}(E, J)$, the additional constraints introduced by the anisotropy of the potential cannot be represented in such a simple manner. Fig. 3 compares the capture probabilities in PST, w^{PST} , with capture probabilities $w(E, J)$ for the anisotropic potential such as derived by the CT calculations. The $\text{C}_8\text{H}_{10}^+$ sys-

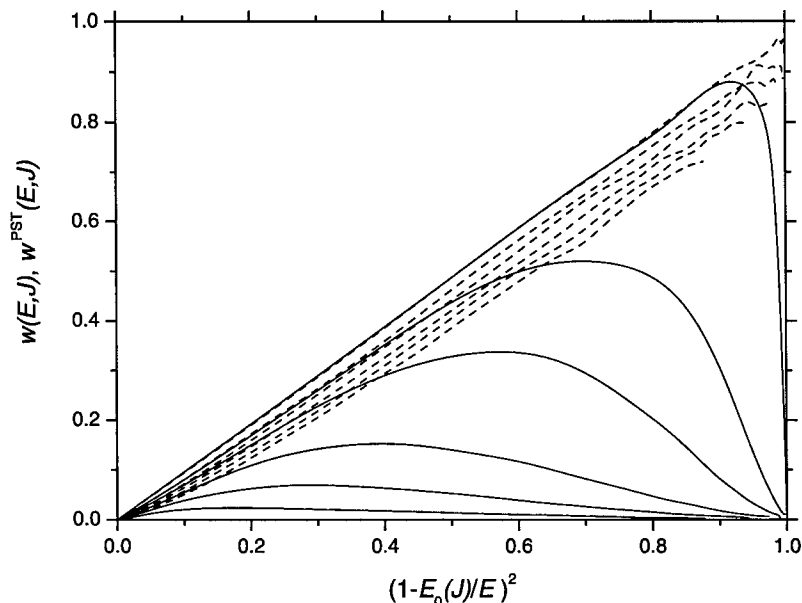


Fig. 4. As Fig. 3 (results for $C_8H_{10}^+$ with ion-dipole type anisotropy with $C_1/D \approx 14$).

tem serves as the example. One observes that, for $J \rightarrow 0$ and $E \rightarrow E_0(J)$, $w(E, J)$ approaches $w^{\text{PST}}(E, J)$. In contrast, for increasing E and J , it falls increasingly below $w^{\text{PST}}(E, J)$. In the language of transition state theory, this would correspond to transition state shifting: with increasing excitation energy, the effective bottle-necks of the dynamics smoothly move to smaller interfragment distances where the potential is more anisotropic [32]. Consequently, $w(E, J)$ falls below $w^{\text{PST}}(E, J)$. An analogous situation applies to angular momentum: with increasing J , the effective bottle-necks of the dynamics smoothly move into a more anisotropic range of the potential. Whereas Fig. 3 illustrates $w(E, J)$ for dipole-dipole type anisotropy, there is practically no change if ion-dipole type anisotropy is chosen instead, as shown by comparing Figs. 3 and 4 (however, the parameters C_1 and C_2 differ). The results for the $C_9H_{12}^+$ system look quite similar and, therefore, are not shown here.

An alternative representation of the consequences of the anisotropy of the PES involves “specific rigidity factors” $f_{\text{rigid}}(E, J)$ defined by

$$f_{\text{rigid}}(E, J) = w(E, J) / w^{\text{PST}}(E, J). \quad (3.7)$$

Fig. 5 demonstrates $f_{\text{rigid}}(E, J)$ for the $C_8H_{10}^+$ system. With increasing energy, $f_{\text{rigid}}(E, J)$ falls increasingly below the PST limit ($f_{\text{rigid}}^{\text{PST}} = 1$). Since $W(E, J)$ for the transitional modes is later convoluted with contributions for conserved modes, only small excitations per mode are of importance for the

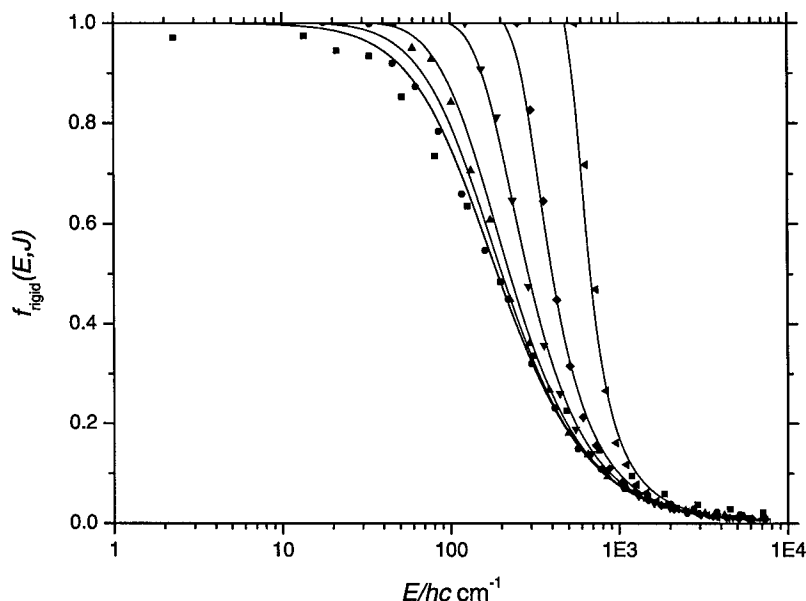


Fig. 5. Specific rigidity factors $f_{\text{rigid}}(E, J)$ for the $\text{C}_8\text{H}_{10}^+$ -system (curves from left to right are for $J = 25, 55, 75, 105, 135$, and 180 , respectively; symbols: results from CT calculations for dipole–dipole type anisotropy with $C_2/D \approx 20$; full curves: analytical approximation by Eq. (3.8) with $m = 2$, $n = -2/3$, and $E_{\text{sw}}/hc \approx 140 \text{ cm}^{-1}$).

polyatomic ions considered here. Therefore, the low energy limiting range of $f_{\text{rigid}}(E, J)$ is most relevant.

For convenience, we have analytically represented the derived $f_{\text{rigid}}(E, J)$ in the form

$$f_{\text{rigid}}(E, J) \approx [1 + \{[E - E_0(J)]/E_{\text{sw}}\}^m]^n. \quad (3.8)$$

It appears worth mentioning that the calculated rigidity factors, except for small $J (\leq 60)$, only depend on $E - E_0(J)$ and do not show additional J -dependences. In addition, the exponents m and n were found to be close to $m \approx 2$ and $n \approx -2/3$. Keeping these values of m and n fixed, the only fit parameter is E_{sw} . Performing the CT calculations for $\text{C}_8\text{H}_{10}^+$ with dipole–dipole anisotropy, $E_{\text{sw}}/hc \approx 140 \text{ cm}^{-1}$ was fitted which corresponds to $C_2/D = 20$. Fig. 5 illustrates the agreement of the CT results and the corresponding empirical fits from Eq. (3.8). Fig. 5 represents the connection between the potential, *e.g.* characterized by dipole–dipole anisotropy and its amplitude factor C_2/D , and the rigidity factor characterized by E_{sw} . We found that E_{sw} is inversely proportional to C_2/D . Empirical fits of Eq. (3.8) and its parameter E_{sw} to experimental results then also lead back to the underlying potential parameter

C_2/D via $C_2/D \approx 20 \times 140 \text{ hc cm}^{-1}/E_{\text{sw}}$. Rigidity factors for $\text{C}_9\text{H}_{12}^+$ were found to look quite similar to those shown in Fig. 5. The corresponding relation for C_2/D was found to be $C_2/D \approx 18 \times 110 \text{ hc cm}^{-1}/E_{\text{sw}}$.

For the large excitations considered in the present work, the classical treatment appears adequate. For smaller excitations, individual adiabatic and axially-nonadiabatic potential curves (including Coriolis coupling) have to be determined as illustrated in [6] and [10]. This difficult task is beyond the scope of the present article. Instead we remain within the SACM/CT concept and convolute $W(E, J)$ from the CT calculations with the contributions from quantized conserved oscillators. It appears most practical to do this by the use of the Beyer–Swinehart algorithm, using the derived analytical expressions for $W(E, J)$ of the transitional modes for the construction of the starting array in the algorithm such as explained in Appendix A of [33]. The frequencies used for the conserved modes of $\text{C}_8\text{H}_{10}^+$ (or $\text{C}_9\text{H}_{12}^+$), corresponding to the vibrations of C_7H_7^+ and CH_3 (or C_2H_5), are listed in Appendix A.

4. Specific rate constants $k(E, J)$

Having calculated $W(E, J)$ and relying on the usual statistical assumption [8] of one-channel rate constants being equal to $1/h\rho(E, J)$, the SACM/CT treatment leads to specific rate constants $k(E, J) = W_{\text{tot}}(E, J) \times [1/h\rho(E, J)]$ as illustrated below. Rovibrational densities of states $\rho(E, J)$ were calculated in the harmonic oscillator-rigid rotor approximation using fundamental frequencies, since it presently is not feasible to properly account for anharmonicity in systems of this size. (Even for triatomic systems, apart from few exceptions, see [34], anharmonic rovibrational densities of states near to the dissociation limit have not yet been determined rigorously). Vibrational densities of states $\rho(E, J = 0)$ were determined by Beyer–Swinehart counting; rotational factors were approximated by the analytical expressions elaborated in [30].

The resulting $k(E, J)$ for the dissociation $\text{C}_8\text{H}_{10}^+ \rightarrow \text{C}_7\text{H}_7^+ + \text{CH}_3$ are shown in Fig. 6. The figure compares PST calculations of $k(E, J)$ with calculations for the anisotropic potential. One realizes a marked influence of the “rigidity of the potential” due to its anisotropy. The reduction of $k(E, J)$ to values below $k^{\text{PST}}(E, J)$ becomes increasingly pronounced with increasing energy: the discrepancy is already a factor of 20–30 at $E/hc = 15\,000 \text{ cm}^{-1}$ and increases to almost three orders of magnitude above $E/hc = 40\,000 \text{ cm}^{-1}$ (one should note that, for Figs. 6, 8, and 10, the zero of the energy scale is the rovibrational ground state of the molecular ion unlike the other figures of this article). The increasing drop of $k(E, J)$ below $k^{\text{PST}}(E, J)$ with increasing energy is the sign of a shifting of the effective dynamical bottle-neck of the reaction towards smaller interfragment distances where the anisotropy is increasingly more pronounced. For a fixed energy E , there is only a weak de-

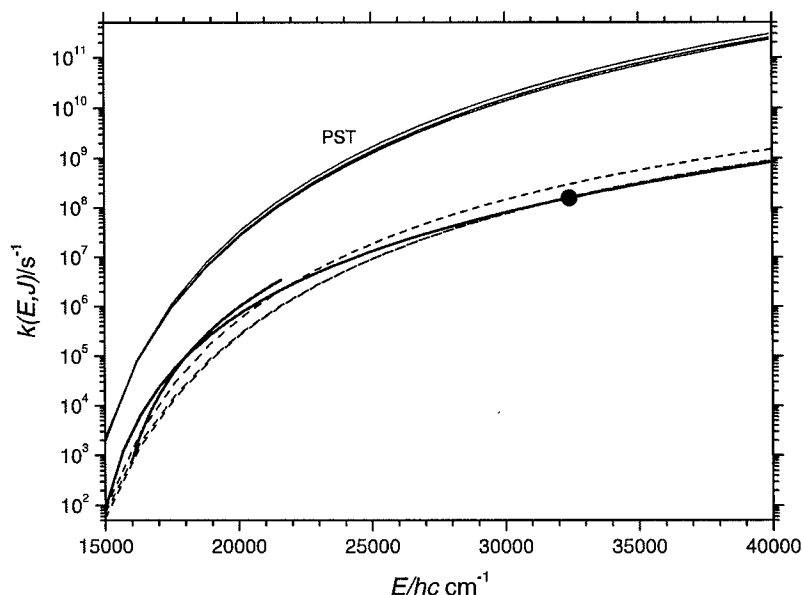


Fig. 6. Specific rate constants $k(E, J)$ for the dissociation $\text{C}_8\text{H}_{10}^+ \rightarrow \text{C}_7\text{H}_7^+ + \text{CH}_3$ (upper full curves: $k^{\text{PST}}(E, J)$ for $J = 0, 65$, and 150 from bottom to top; lower dashed curves: $k(E, J)$ for $J = 0$ (middle), 65 (bottom), and 150 (top), see text; for a more detailed representation of the J -dependence, see Fig. 7; full circle: experimental result from [37]; full curve between $E = 16000$ and 22000 cm^{-1} : experimental results from [38]; full curve from $k(E, J) = 10^2$ to 10^9 s^{-1} : empirical fitting of experimental results by Eq. (6.2), see text).

pendence of $k(E, J)$ on J . This is shown in Fig. 6 and illustrated on a larger scale in Fig. 7. The weakness of the J -dependence corresponds to that calculated for the fragmentations of neutral toluene and ethylbenzene [35] and also to the experimental results obtained for the fragmentation of benzene cations [36]. $k^{\text{PST}}(E, J)$ shows the same J -dependence as $k(E, J)$ such that the J -dependence of $f_{\text{rigid}}(E, J)$ is not responsible for the calculated trends. Since three unrelated factors, *i.e.* the J -dependences of $W^{\text{PST}}(E, J)$, of $\rho(E, J)$, and of $E_0(J)$, govern the J -dependence of $k(E, J)$, there is no simple explanation for the resulting J -dependence.

The model potentials discussed in Sect. 2 contain a number of quantities that needed to be fixed before the CT calculations were made. Apart from the known molecular parameters given in Appendix A, the Morse parameters β as well as the anisotropy amplitudes C_1/D or C_2/D had to be specified. Whereas β could be related to a vibration defining the reaction coordinate, C_1/D or C_2/D were parameters fitted through a comparison of the calculated $k(E, J)$ with experimental results. As a first guess of the order of magnitude we have

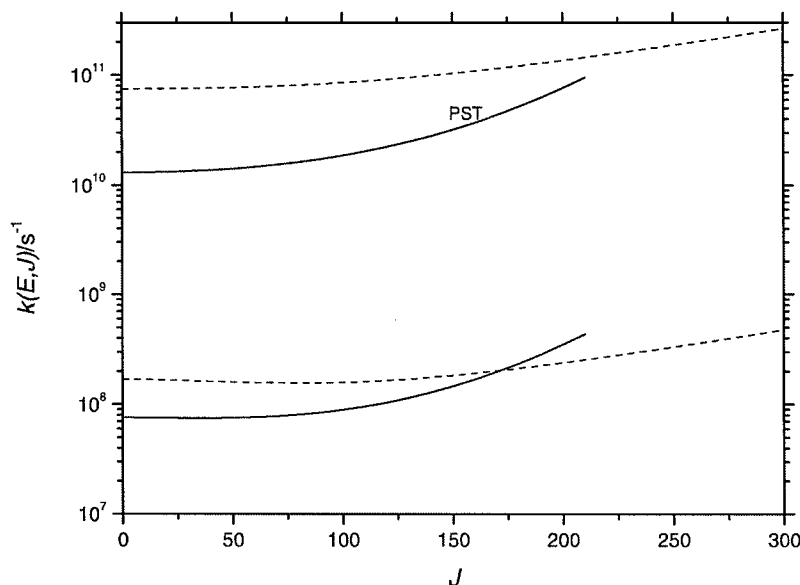


Fig. 7. J -dependence of $k(E, J)$ and $k^{\text{PST}}(E, J)$ for the dissociations $\text{C}_8\text{H}_{10}^+ \rightarrow \text{C}_7\text{H}_7^+ + \text{CH}_3$ (full lines) and $\text{C}_9\text{H}_{12}^+ \rightarrow \text{C}_7\text{H}_7^+ + \text{C}_2\text{H}_5$ (dashed lines) (modelling results for PST (upper curves) and for anisotropic potential (lower curves) at $E/hc = 30\,000\text{ cm}^{-1}$).

estimated these parameters by means of the anisotropy parameters from the Appendix of [6]. In this way, we choose $C_2/D \approx 20$ for $\text{C}_8\text{H}_{10}^+$. This value was used for the illustrative examples of the CT calculations in Figs. 3–5. However, this value of C_2/D gives $k(E, J)$ which differ from the measurements. In order to obtain a more realistic C_2/D , the corresponding E_{sw} in Eq. (3.8) was varied until an optimum experimental value of $k(E)$ was reproduced. Choosing the experimental $k(E)$ near $32\,000\text{ cm}^{-1}$ from [37] for this purpose, the fit parameters $E_{\text{sw}}/hc \approx 38\text{ cm}^{-1}$ and $C_2/D \approx 74$ are obtained. In this way the complete $k(E, J)$ is predicted as shown in Figs. 6 and 7. The low energy results near $18\,000\text{ cm}^{-1}$ from [38] are not well reproduced, predicting a slightly different energy dependence of $k(E)$. However, the differences still appear to be within the uncertainties of both the experiments and the model potential. Better agreement would be obtained by slightly lowering the value of E_0 which is not well known. In addition, the disagreement is in the range of $k(E)$ where radiative cooling may be important. This is not modelled here.

Modelled $k(E, J)$ for the dissociation $\text{C}_9\text{H}_{12}^+ \rightarrow \text{C}_7\text{H}_7^+ + \text{C}_2\text{H}_5$ are compared with measured $k(E)$ from [39] in Fig. 8. In this case, dipole–dipole anisotropies from Eq. (2.16) were used in CT calculations with starting values of $C_2/D = 18$ which were found to correspond to $E_{\text{sw}}/hc = 110\text{ cm}^{-1}$ in

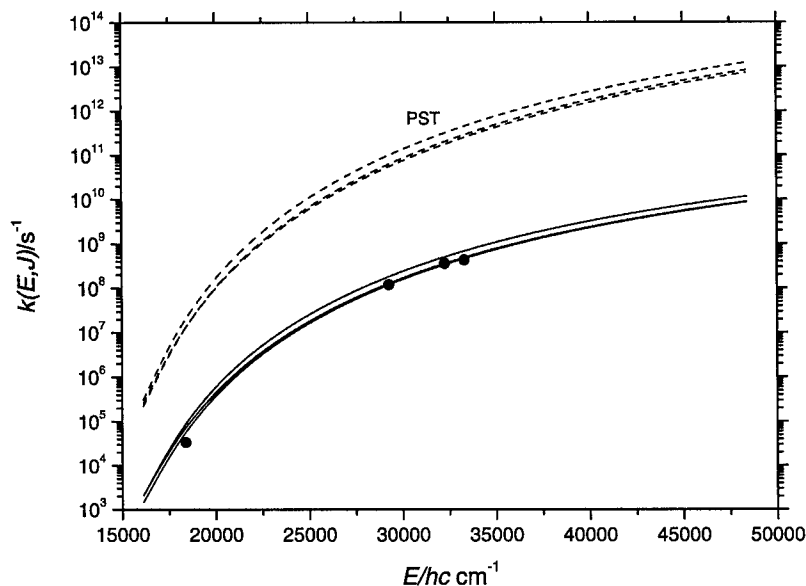


Fig. 8. As Fig. 6, for the dissociation $\text{C}_9\text{H}_{12}^+ \rightarrow \text{C}_7\text{H}_7^+ + \text{C}_2\text{H}_5$ (upper dashed curves: $k^{\text{PST}}(E, J)$ for $J = 0, 100$, and 200 from bottom to top; lower full curves: $k(E, J)$ for $J = 0$ (middle), 100 (bottom), and 200 (top); see text; full circles: experimental results from [39]).

Eq. (3.8). The fit to the experiments then was done choosing the experimental point from [39] near $32\,000\text{ cm}^{-1}$ which fixes $E_{\text{sw}}/hc \approx 17.3\text{ cm}^{-1}$. This value again is smaller than the starting value of our CT calculations and corresponds to $C_2/D \approx 114$. The complete $k(E, J)$ is constructed, in this case agreeing very well with the low energy point near $18\,000\text{ cm}^{-1}$. The modelled J -dependences of $k(E, J)$ show the same trends as observed for $\text{C}_8\text{H}_{10}^+$ as shown in Fig. 7. The shape of the J -dependence of $k(E, J)$ slightly differs from that obtained for $\text{C}_8\text{H}_{10}^+$. The details of this trend are again caused by a complicated interplay of $\rho(E, J)$, of $W^{\text{PST}}(E, J)$, and of $E_0(J)$. More practical aspects of the modelled $k(E, J)$ are discussed below.

5. Thermal capture rate constants $k_{\text{cap}}(T)$

The number of open channels $W(E, J)$ also forms the basis for the calculation of thermal capture and high pressure association rate constants. For example, the PST expression of Eq. (2.14) with the centrifugal pseudo-partition function of Eq. (2.13) and the centrifugal barriers from Eq. (2.11) leads to the Langevin expression $k_{\text{cap}}^{\text{PST}} = k_{\text{L}} = 2\pi q(\alpha/\mu)^{1/2}$ for ion-induced dipole capture, see above.

For the present short-range valence/long-range induced dipole potentials, a number of changes arise: (i) the PST capture rate constant from Eq. (2.14) has to be calculated with $E_0(J)$ from Eq. (2.10) instead of Eq. (2.11), (ii) the general capture rate constants $k_{\text{cap}}(T)$ have to account for the specific rigidity factors of Eq. (3.8), (iii) one has to check whether the frequencies of the conserved modes can be identified with the frequencies of the separated fragments, and (iv) one has to relate $k_{\text{cap}}(T)$ with experimental high pressure association rate constants $k_{\text{rec},\infty}(T)$ by inspecting which fraction of the electronic states of the separated fragments leads to the bound adduct under consideration. In the simplest case, the latter relation is established by

$$k_{\text{rec},\infty}(T) = k_{\text{cap}}(T) Q_{\text{el}}(A) / [Q_{\text{el}}(B) Q_{\text{el}}(C)], \quad (5.1)$$

where Q_{el} are the respective electronic partition functions of $A \rightleftharpoons B + C$. Assumption (iii) often is true to a sufficient extent, because the major part of changes of conserved mode frequencies from A to $B + C$ will generally occur at shorter distances than relevant for the effective bottle-necks of the transitional mode dynamics, see the original version of SACM [13]. In this case, the calculation of k_{cap} will only concern transitional modes, *i.e.*

$$k_{\text{cap}}(T) = \frac{kT}{h} \left(\frac{h^2}{2\pi\mu kT} \right)^{3/2} \frac{Q^*}{Q_{\text{rot}}(B) Q_{\text{rot}}(C)} \quad (5.2)$$

with the pseudo-partition function Q^* given by

$$Q^* = \sum_{J=0}^{\infty} (2J+1) \int_{E_0(J)}^{\infty} W(E, J) \exp(-E/kT) dE/kT \quad (5.3)$$

where $W(E, J)$ here is the number of open channels of the transitional modes and Q_{rot} are the rotational partition functions of the separated fragments B and C , respectively.

Evaluating $k_{\text{cap}}^{\text{PST}}(T)$ for the capture $\text{C}_7\text{H}_7^+ + \text{CH}_3 \rightarrow \text{C}_8\text{H}_{10}^+$ with Eqs. (2.10), (2.13), and (2.14) leads to the results shown in Fig. 9. $k_{\text{cap}}^{\text{PST}}(T)$ increases slightly from the Langevin rate constant at low temperatures to larger values at higher temperatures which reflects the stronger attraction of the short-range/long-range switching potential of Sect. 2.1 in comparison to a pure ion-induced dipole potential. Including the specific rigidity factors $f_{\text{rigid}}(E, J)$ from Eq. (3.8) in Eqs. (5.2) and (5.3) leads to the curve for $k_{\text{cap}}(T)$ in Fig. 9 which falls increasingly below $k_{\text{cap}}^{\text{PST}}(T)$ with increasing temperature. Again this reflects a shifting of the effective bottle-necks of the transitional mode dynamics into the more anisotropic short-range valence portion of the PES. It should be emphasized that Fig. 9 shows thermal capture rate constants which are fully consistent with the specific rate constants $k(E, J)$ from Fig. 6.

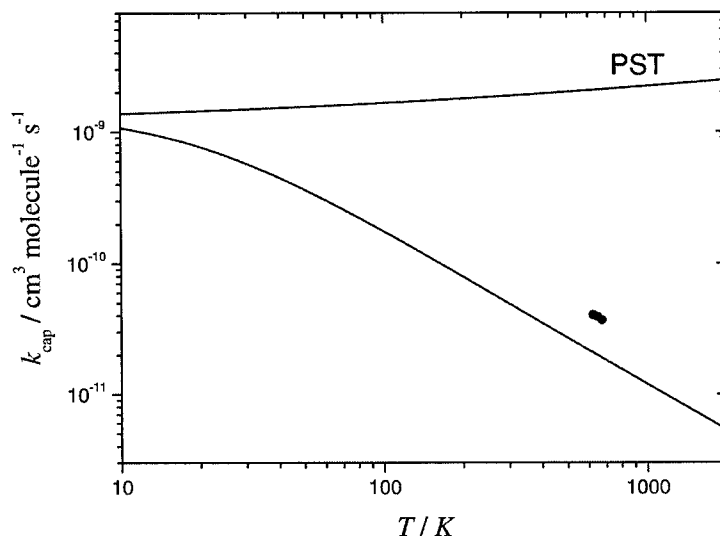


Fig. 9. Thermal capture rate constants $k_{\text{cap}}(T)$ for the reaction $\text{C}_7\text{H}_7^+ + \text{CH}_3 \rightarrow \text{C}_8\text{H}_{10}^+$ (upper curve: PST, CT calculations and Eqs. (2.10), (2.13), and (2.14); lower curve: k_{cap} , CT calculations and calculations with Eq. (3.8) fitted to reproduce $k(E, J)$ from Fig. 8, see text; empirical representation by Eq. (7.2) with $T_0 = 30.4$ K; \bullet : experimental points from dissociation experiments converted by the equilibrium constant from [43]).

6. Simplified modelling of $k(E, J)$

The above treatment of the dynamics on the level of the SACM/CT concept provides an accurate connection between $k(E, J)$ and the PES. In the following we also compare these results with a series of simpler procedures which may be of practical use. Since one has to fit potential parameters in any case, one may also ignore the potential from the beginning and fit $k(E, J)$ to a limited number of experimental points. This appears desirable when $k(E)$ has to be extrapolated and, in particular, when kinetic shifts have to be determined in order to derive bond energies E_0 from $k(E)$. It was suggested in [40] that $k(E)$, for polyatomic dissociating species, can be approximated by an expression

$$k(E) \approx A^* (E - E_0)^{s^* - 1} \quad (6.1)$$

with the true bond energy E_0 , an empirical exponent $s^* - 1$ and a constant factor A^* . The form of Eq. (6.1) should be distinguished from classical Kassel theory which has an additional energy dependence in the denominator and identifies s^* with the number of activated complex oscillators. After rewriting Eq. (6.1) in the form

$$k(E) \approx A[(E - E_0)/(E_{\text{ref}} - E_0)]^{s^* - 1}, \quad (6.2)$$

we find, for $\text{C}_8\text{H}_{10}^+ \rightarrow \text{C}_7\text{H}_7^+ + \text{CH}_3$, that $k(E)$ could well be represented with $A = 1.6 \times 10^8 \text{ s}^{-1}$, $E_0/hc = 14\,070 \text{ cm}^{-1}$, $E_{\text{ref}}/hc = 32\,420 \text{ cm}^{-1}$, and $s^* = 5.962$, using the measured $k(E)$ at E_{ref} from [37] as the reference fitting point and using the experimental results from [38] for fixing s^* . As seen in Fig. 6, a slightly steeper energy dependence of $k(E)$ over the range $16\,000\text{--}21\,000 \text{ cm}^{-1}$ in [38] was determined experimentally than given by Eq. (6.2). While the fully empirical Eqs. (6.1) and (6.2) do a fair job in reproducing measured and calculated $k(E, J = 0)$, the J -dependence of $k(E, J)$ escapes a simple empirical representation. In any case, the weak J -dependence illustrated in Fig. 7 indicates that the measured $k(E)$ from [37] and [38] are not different from $k(E, J = 0)$ within experimental error.

Comparison of the simplified SACM calculations of $k(E, J = 0)$ for the dissociations of neutral toluene to benzyl + H or phenyl + CH_3 and of ethylbenzene to benzyl + CH_3 [35] to results obtained with pure model valence potentials confirms the good performance of Eq. (6.1). In those cases, J -dependences of $k(E, J)$ were determined with increasing $k(E, J)$ for increasing J in C–C bond breaking, like in the present work, and decreasing $k(E, J)$ in C–H bond breaking [35], in contrast to the present work.

Reliable experimental values of $k(E)$ at three energies are enough to determine the three empirical parameters in Eq. (6.1) and therefore sufficient to derive E_0 . For a less empirical approach and for a determination of E_0 , two sufficiently distant experimental points of $k(E)$ would suffice if $k(E, J)$ from a PST calculation is combined with $f_{\text{rigid}}(E, J)$ from Eq. (3.8) and the two parameters E_0 and E_{SW} are fitted. While the full SACM/CT treatment requires large computing efforts, this simple “modified PST treatment” is by far less time consuming. Including centrifugal barriers $E_0(J)$ as defined in Eq. (2.10) into the PST treatment, allows the correct J -dependence of $k(E, J)$ to also be satisfactorily accounted for.

Common practice is to model $k(E, J = 0)$ with RRKM theory using oscillator-type activated complexes, see e.g. [8, 37, 39]. Because of the large number of adjustable frequencies, this approach can obviously also reproduce measured $k(E)$. However, there is no rigorous justification for this procedure in simple bond fissions without reverse barriers, and the chosen frequencies of the transitional modes have no direct relation to the properties of the potential. Fixing the frequencies of the conserved modes to those of the fragment modes, one might try in RRKM theory to treat the transitional modes as rotors, such as done in PST. However this causes apparent increases of the rotational constants in order to mimic rigidity [41]. Fitting this increase would lead to an energy independent rigidity factor which obviously does not correspond to the results for $k(E, J)$ shown in Figs. 6 and 8. A microcanonical VRC-VTST-treatment [18] of the transitional modes (see above), of course, would produce better results. However, it also requires a full reduced-dimensionality PES, is fairly involved, requires dynamical corrections [19], and needs parameter fitting as long as no *ab initio* potential is available.

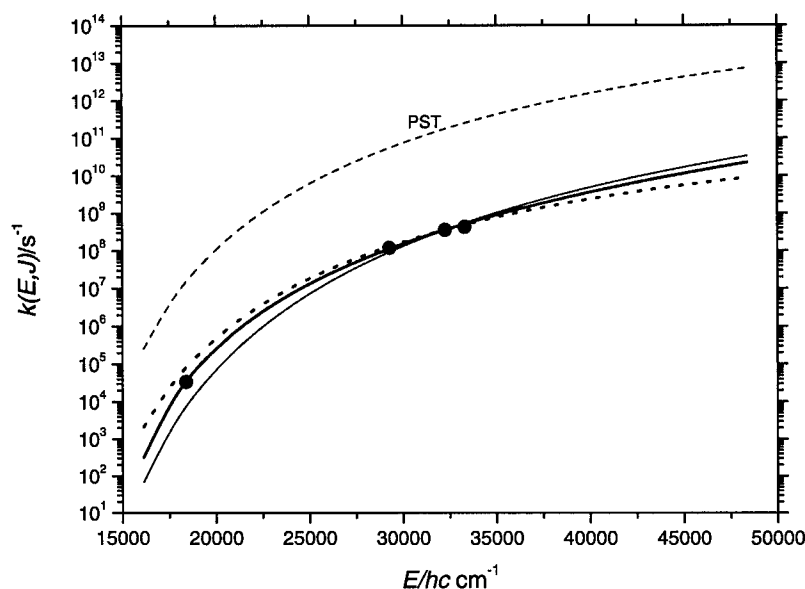


Fig. 10. Simplified representations of specific rate constants $k(E, J = 0)$ for the dissociation $\text{C}_9\text{H}_{12}^+ \rightarrow \text{C}_7\text{H}_7^+ + \text{C}_2\text{H}_5$ (see Fig. 8, experimental points from [39]; heavy full line: empirical fit by Eq. (6.2) with $A = 3.6 \times 10^8 \text{ s}^{-1}$, $E_0/hc = 13\,950 \text{ cm}^{-1}$, $E_{\text{ref}}/hc = 32\,260 \text{ cm}^{-1}$ and $s^* = 7.541$; light full line: RRKM fit from [39]; dotted line: SACM/CT modelling adjusted to the experimental point near $32\,000 \text{ cm}^{-1}$ and represented by modified PST calculation with Eq. (3.8) with $E_{\text{sw}}/hc = 17.3 \text{ cm}^{-1}$; dashed line: PST calculation).

Fig. 10 compares $k(E, J = 0)$ from the various approaches for the reaction of $\text{C}_9\text{H}_{12}^+ \rightarrow \text{C}_7\text{H}_7^+ + \text{C}_2\text{H}_5$. Included in this figure are an empirical fit using Eq. (6.2), a modified PST modelling using Eq. (3.8) being equivalent to the full SACM/CT results, an RRKM fit from [39], and the experimental points from [39]. The differences of the different approaches become clearly visible only when larger energy ranges are considered. However, larger energy ranges generally are relevant when kinetic shifts of specific rate constants are estimated [8]. Therefore, the different simplified methods described in this section may also lead to different results among each others and differ from the detailed SACM/CT results.

7. Simplified modelling of $k_{\text{cap}}(T)$

After having presented simplified ways to characterize $k(E, J)$, one may also try to represent $k_{\text{cap}}(T)$ in a simple manner that is consistent with the simplified $k(E, J)$. For the $\text{C}_8\text{H}_{10}^+$ system, the decrease with increasing tempera-

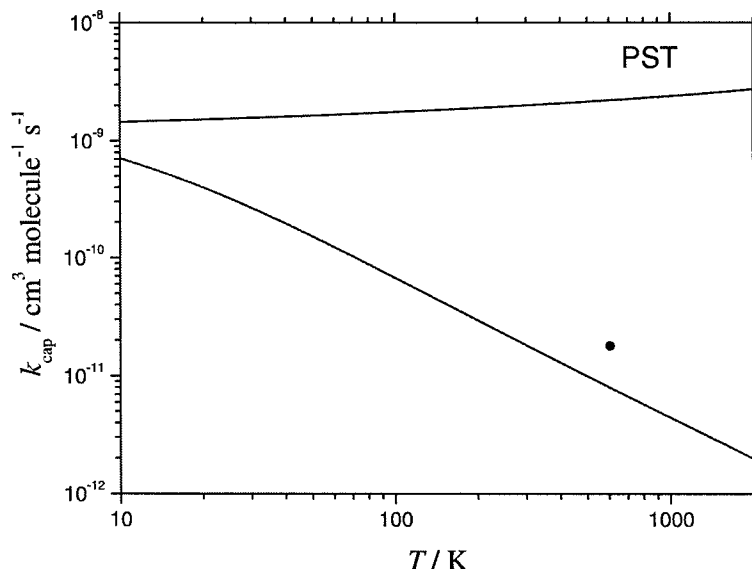


Fig. 11. As Fig. 9, but for $\text{C}_7\text{H}_7^+ + \text{C}_2\text{H}_5 \rightarrow \text{C}_9\text{H}_{12}^+$ (upper curve: PST; lower curve: k_{cap} corresponding to $k(E, J)$ from Fig. 8; experimental point at 603 K from high pressure dissociation experiments of $\text{C}_9\text{H}_{12}^+$ after conversion by the equilibrium constant [42]; empirical representation by Eq. (7.2) with $T_0 = 13.8$ K; minor changes of the employed equilibrium constant would bring the point and Eq. (7.2) into agreement, see [42]).

tures of the capture rate constants from values dominated by the long-range electrostatic potential to values dominated by the short-range valence component of the potential is shown in Fig. 9. Similar results were obtained for the $\text{C}_9\text{H}_{12}^+$ system and are illustrated in Fig. 11. As a result of the anisotropy of the potential, which is calibrated by the measurements of $k(E)$, k_{cap} falls markedly below the results from PST in both cases. Before asking whether this prediction is confirmed by experiments, we try to provide an analytical expression for $k_{\text{cap}}(T)$ which is linked to the values of E_{sw} characterizing $k(E, J)$. Calculating $k_{\text{cap}}(T)$ for the short-range potential separately would lead to $k_{\text{cap}}^{\text{SR}}(T)$. One may expect that this is the limit of $k_{\text{cap}}(T)$ approached at high temperatures while $k_{\text{cap}}^{\text{PST}}(T)$ is the limit approached at low T . We found that the transition between $k_{\text{cap}}^{\text{PST}}(T)$ and $k_{\text{cap}}^{\text{SR}}(T)$ then can be approximated by

$$k_{\text{cap}}(T) \approx k_{\text{cap}}^{\text{SR}}(T) + [k_{\text{cap}}^{\text{PST}}(T) - k_{\text{cap}}^{\text{SR}}(T)] [T_0 / (T_0 + T)]^{1.5}. \quad (7.1)$$

As $k_{\text{cap}}^{\text{PST}}(T) \gg k_{\text{cap}}^{\text{SR}}(T)$ in the present case, Eq. (7.1) simplifies to

$$k_{\text{cap}}(T) \approx k_{\text{cap}}^{\text{PST}}(T) [T_0 / (T_0 + T)]^{1.5}. \quad (7.2)$$

In contrast to the value 1.5 of the exponent, we found empirically that the parameter T_0 is linked to E_{SW} by

$$kT_0 \approx 0.56E_{\text{SW}} \quad (7.3)$$

where E_{SW} is from Eq. (3.8). E_{SW} is determined either through theoretical modelling or through empirical fitting of $k(E)$. Eqs. (7.1)–(7.3) then provide the internally consistent link between $k(E)$ and $k_{\text{cap}}(T)$. At the same time, through the connection between T_0 , E_{SW} , and C_2/D , the link to the dominant parameter characterizing the anisotropy of the potential is established.

The prediction that thermal rate constants for capture of CH_3 or C_2H_5 by C_7H_7^+ are far below the Langevin rate constants for ion-induced dipole capture needs experimental verification. The corresponding experiments have not yet been made for the recombination process. However, recent turbulent ion flow tube (TIFT) measurements of the rate of pyrolysis of $\text{C}_8\text{H}_{10}^+$ and of $\text{C}_9\text{H}_{12}^+$ have been reported in [42] and [43]. These experiments have been made very near to the high pressure limit of the unimolecular dissociation. Converting these results by the equilibrium constant to the high pressure recombination rate constant, one obtains $k_{\text{rec},\infty}$ which in this case indeed are close to k_{cap} as derived from the measured $k(E)$. The corresponding results are included in Figs. 9 and 11. The near agreement confirms the internal consistency of the present approach, *i.e.* the measured thermal dissociation rates are consistent with the experimental specific rate constants and both quantities can be related to the relevant potential parameters. The small differences may be explained by experimental uncertainties either of $k(E)$ or of $k_{\text{diss}}(T)$, or by E_0 which enters the equilibrium constants.

8. Conclusions

In the present work specific rate constants $k(E, J)$ and thermal capture rate constants $k_{\text{cap}}(T)$ for representative examples of molecular ion dissociations and the reverse associations have been calculated in a consistent way by the SACM/CT approach. Model potentials of mixed short-range valence and long-range electrostatic character were employed and direct links between rate constants and potential parameters were established. The chosen examples $\text{C}_8\text{H}_{10}^+$ and $\text{C}_9\text{H}_{12}^+$ are characterized by small Massey parameters for the transitional modes such that their dynamics is nonadiabatic. The same is true for a large series of other neutral or ion dissociations and recombinations such as $\text{H} + \text{CH}_3 \rightleftharpoons \text{CH}_4$ ($\xi = 0.35$), $\text{H} + \text{C}_2\text{H}_3 \rightleftharpoons \text{C}_2\text{H}_4$ ($\xi = 0.12$), $\text{H} + \text{C}_2\text{H}_5 \rightleftharpoons \text{C}_2\text{H}_6$ ($\xi = 0.088$) or $2\text{CH}_3 \rightleftharpoons \text{C}_2\text{H}_6$ ($\xi = 0.95$), $2\text{C}_2\text{H}_5 \rightleftharpoons \text{C}_4\text{H}_{10}$ ($\xi = 0.36$), and $2\text{C}_7\text{H}_7 \rightleftharpoons \text{C}_{14}\text{H}_{14}$ ($\xi = 0.21$), $\text{NC} + \text{NO} \rightarrow \text{NCNO}$ ($\xi = 0.43$), $\text{C}_6\text{H}_5^+ + \text{H} \rightarrow \text{C}_6\text{H}_6^+$ ($\xi = 0.053$), and $\text{C}_6\text{H}_5^+ + \text{Br} \rightarrow \text{C}_6\text{H}_5\text{Br}^+$ ($\xi = 0.20$). If these reactions were treated by VTST, *i.e.* through phase space sampling along

c.o.m. reaction coordinates, dynamical corrections for nonadiabaticity would have to be applied, see [19] and [44].

As *ab initio* calculations of the potential for molecular ions of the size considered here are only rarely available with adequate precision, some potential parameters in general have to be fit. In this situation it may suffice to do a parameter fitting directly to empirical expressions representing the experimental data. We have proposed several simple ways which minimize the number of fit parameters. These have been validated by comparison with the full dynamical SACM/CT treatment. $k(E, J)$ and $k_{\text{cap}}(T)$ for both the full theoretical treatment and the simplified parametrized level were determined in a consistent manner. In this way, the consequences of having a short-range valence and long-range electrostatic character of the potential could be elaborated in detail. A consequence of the marked anisotropy of the short-range valence potential are specific rate constants $k(E, J)$ which are far below the predictions from phase space theory. Likewise, thermal recombinations of CH_3 and C_2H_5 with C_7H_7^+ are predicted to have rate constants far below the Langevin rate constant in the high pressure limit. The latter prediction was confirmed by pyrolysis experiments of $\text{C}_8\text{H}_{10}^+$ and $\text{C}_9\text{H}_{12}^+$. Finally, the SACM/CT calculations of the present work have been complemented by product energy distributions in [22] which are internally consistent with the present results for $k(E, J)$ and $k_{\text{cap}}(T)$.

Acknowledgement

Many discussions of our work with Professor Jürgen Wolfrum over many years are gratefully acknowledged.

Financial support by the Deutsche Forschungsgemeinschaft (SFB 357 "Molekulare Mechanismen unimolekularer Reaktionen"), by the Air Force Office of Scientific Research (task number 2303EP4), and by the European Office of Aerospace Research and Development (Award No. FA8655-03-1-3034) are also gratefully acknowledged.

Appendix: Molecular parameters

a) $\text{C}_8\text{H}_{10}^+ \rightarrow \text{C}_7\text{H}_7^+ + \text{CH}_3$ (parameters taken from [37] and [38]):

$E_0/hc = 14\,070 \text{ cm}^{-1}$; $B_i(\text{C}_7\text{H}_7^+)/hc = 0.18, 0.094, \text{ and } 0.062 \text{ cm}^{-1}$; $\sigma(\text{C}_7\text{H}_7^+) = 2$; $B_i(\text{CH}_3)/hc = 9.3, 9.3, \text{ and } 4.65 \text{ cm}^{-1}$; $\sigma(\text{CH}_3) = 6$; Morse parameter $\beta = hc\omega\sqrt{\mu}/2\hbar^2 E_0 = 3.68 \text{ \AA}^{-1}$ with $\omega = 1003 \text{ cm}^{-1}$; $r_e = 3.46 \text{ \AA}$; $\alpha(\text{CH}_3) = 2.334 \text{ \AA}^3$ from [45]; frequencies $\omega_i/\text{cm}^{-1} = 163, 337, 342, 407, 510, 582, 611, 628, 778, 782, 843, 946, 963, 976, 1000, 1012, 1046, 1089, 1112, 1134, 1157, 1307, 1311, 1326, 1420, 1452, 1540, 1547, 1583, 2975, 3011, 3015, 3017, 3036, 3039, 3067$ for C_7H_7^+ , and $304, 1365, 1365, 2911, 3072, 3072$ for CH_3 ; $\beta r_e = 12.73$, $\beta r_{\text{Be}} = 7.123$, $\beta r_{\text{SW}} = 14.186$, $\alpha q^2 \beta^4 / 2D = 1743$.

b) $\text{C}_9\text{H}_{12}^+ \rightarrow \text{C}_7\text{H}_7^+ + \text{C}_2\text{H}_5$ (parameters taken from a) and from [39] and [42]):
 $E_0/hc = 13\,950\text{ cm}^{-1}$; $B_i(\text{C}_2\text{H}_5)/hc = 3.51, 0.75$, and 0.70 ; $\sigma(\text{C}_2\text{H}_5) = 1$;
 Morse parameter $\beta = 5.13\text{ \AA}^{-1}$ with $\omega = 1061\text{ cm}^{-1}$; $r_e = 4.74\text{ \AA}$; $\alpha(\text{C}_2\text{H}_5) = 4.27\text{ \AA}^3$ from [45]; frequencies $\omega_i/\text{cm}^{-1} = 155, 316, 784, 963, 997, 1166, 1383, 1437, 1448, 1459, 2839, 2876, 2925, 2970, 3064$ for C_2H_5 ; $\beta r_e = 24.32$,
 $\beta r_{\text{Be}} = 12.43$, $\beta r_{\text{SW}} = 26.34$, $\alpha q^2 \beta^4 / 2D = 12\,300$.

References

1. A. I. Maergoiz, E. E. Nikitin, J. Troe, and V. G. Ushakov, *J. Chem. Phys.* **105** (1996) 6263.
2. A. I. Maergoiz, E. E. Nikitin, J. Troe, and V. G. Ushakov, *J. Chem. Phys.* **105** (1996) 6270.
3. A. I. Maergoiz, E. E. Nikitin, J. Troe, and V. G. Ushakov, *J. Chem. Phys.* **105** (1996) 6277.
4. A. I. Maergoiz, E. E. Nikitin, J. Troe, and V. G. Ushakov, *J. Chem. Phys.* **108** (1998) 5265.
5. A. I. Maergoiz, E. E. Nikitin, J. Troe, and V. G. Ushakov, *J. Chem. Phys.* **108** (1998) 9987.
6. A. I. Maergoiz, E. E. Nikitin, J. Troe, and V. G. Ushakov, *J. Chem. Phys.* **117** (2002) 4201.
7. J. Troe, *J. Chem. Soc. Faraday Trans.* **90** (1994) 2303.
8. T. Baer and W. L. Hase, *Unimolecular Reaction Dynamics, Theory and Experiments*, Oxford University Press, New York and Oxford (1996).
9. E. I. Dashevskaya, A. I. Maergoiz, J. Troe, I. Litvin, and E. E. Nikitin, *J. Chem. Phys.* **118** (2003) 7313.
10. E. I. Dashevskaya, I. Litvin, E. E. Nikitin, and J. Troe, *J. Chem. Phys.* **120** (2004) 9984.
11. D. C. Clary, T. S. Stoecklin, and A. G. Wickham, *J. Chem. Soc. Faraday Trans.* **89** (1993) 2185.
12. A. I. Maergoiz, E. E. Nikitin, and J. Troe, *Z. Phys. D* **36** (1996) 339; J. Troe, *J. Chem. Phys.* **105** (1996) 6249.
13. M. Quack and J. Troe, *Ber. Bunsenges. Phys. Chem.* **78** (1974) 240.
14. D. M. Wardlaw and R. A. Marcus, *J. Chem. Phys.* **89** (1988) 4761; S. J. Klippenstein and R. A. Marcus, *J. Chem. Phys.* **91** (1989) 2280.
15. J. Troe and V. G. Ushakov, *J. Chem. Phys.* **115** (2001) 3621.
16. M. I. Lester, B. V. Pond, D. T. Anderson, L. B. Harding, and A. F. Wagner, *J. Chem. Phys.* **113** (2002) 9889; M. I. Lester, B. V. Pond, M. D. Marshall, D. T. Anderson, L. B. Harding, and A. F. Wagner, *Faraday Discuss. Chem. Soc.* **118** (2001) 373; H.-G. Yu, J. T. Muckermann, and T. J. Sears, *Chem. Phys. Lett.* **344** (2001) 547.
17. L. B. Harding, *J. Phys. Chem.* **93** (1989) 8004; **95** (1991) 8653; B. Kuhn, T. R. Rizzo, D. Luckhaus, M. Quack, and M. A. Suhm, *J. Chem. Phys.* **111** (1999) 2565; J. Troe, *Chem. Rev.* **103** (2003) 4565; J. Troe and V. G. Ushakov, *Phys. Chem. Chem. Phys.* (2005), submitted.
18. L. B. Harding and S. J. Klippenstein, *Proc. Combust. Inst.* **27** (1998) 151; **28** (2000) 1503; S. J. Klippenstein and B. Harding, *J. Phys. Chem. A* **103** (1999) 9388; *Phys. Chem. Chem. Phys.* **1** (1999) 989.
19. S. J. Klippenstein, Y. Georgievskii, and L. B. Harding, *Proc. Combust. Inst.* **29** (2002) 1229; L. B. Harding, S. J. Klippenstein, and Y. Georgievskii, *Proc. Combust. Inst.* **30** (2004), in press.

20. W. J. Chesnavich, T. Su, and M. T. Bowers, *J. Chem. Phys.* **72** (1980) 2641; D. A. Webb and W. J. Chesnavich, *J. Phys. Chem.* **87** (1983) 3791; W. J. Chesnavich, *J. Chem. Phys.* **84** (1986) 2615.
21. X. Hu and W. L. Hase, *J. Phys. Chem.* **93** (1989) 6029.
22. J. Troe, V. G. Ushakov, and A. A. Viggiano, *Z. Phys. Chem.* **219** (2005) 699.
23. P. Pechukas and J. C. Light, *J. Chem. Phys.* **42** (1965) 3281; E. E. Nikitin, *Theor. Exp. Chem.* **1** (1965) 90.
24. W. J. Chesnavich and M. T. Bowers, *J. Am. Chem. Soc.* **98** (1976) 8301; **99** (1977) 1705; *J. Chem. Phys.* **66** (1977) 2306.
25. S. J. Klippenstein, *Int. J. Mass Spectrom. Ion Process.* **167/168** (1997) 235.
26. W. A. Lester, *J. Chem. Phys.* **53** (1970) 1511; **54** (1971) 3171; **57** (1972) 3028; W. Kutzelnigg, V. Staemmler, and K. Hoheisel, *Chem. Phys.* **1** (1973) 27; J. Troe, *J. Phys. Chem.* **90** (1986) 3485.
27. C. Léonard, P. Rosmus, S. Carter, and N. C. Handy, *J. Phys. Chem. A* **103** (1999) 1846; J. Troe, *Phys. Chem. Chem. Phys.* **7** (2005), in press.
28. J. Troe, *J. Chem. Phys.* **79** (1983) 6017.
29. T. Su and W. J. Chesnavich, *J. Chem. Phys.* **76** (1982) 5183; W. J. Chesnavich and M. T. Bowers, *Gas Phase Ion Chemistry, Vol. 1*, M. T. Bowers (ed.), Academic Press, New York (1979), p. 119.
30. M. Olzmann and J. Troe, *Ber. Bunsenges. Phys. Chem.* **96** (1992) 1327; **98** (1994) 1563.
31. C. E. Klots and J. Polach, *J. Phys. Chem.* **99** (1995) 15396.
32. M. Quack and J. Troe, *Ber. Bunsenges. Phys. Chem.* **81** (1977) 329.
33. D. C. Astholz, J. Troe, and W. Wieters, *J. Chem. Phys.* **70** (1979) 5107.
34. R. F. Salzgeber, V. A. Mandelshtam, and C. Schlier, *J. Chem. Phys.* **110** (1999) 3756; H. Zhang and S. Smith, *J. Chem. Phys.* **120** (2004) 9583.
35. U. Brand, H. Hippler, L. Lindemann, and J. Troe, *J. Phys. Chem.* **94** (1990) 6305; K. Luther, J. Troe, and K.-M. Weitzel, *J. Phys. Chem.* **94** (1990) 6316.
36. A. Kiermeier, H. Kühlewind, H. J. Neusser, E. W. Schlag, and S. H. Lin, *J. Chem. Phys.* **88** (1988) 6182.
37. Y. H. Kim, J. C. Choe, and M. S. Kim, *J. Phys. Chem. A* **105** (2001) 5751.
38. M. Malow, M. Penno, and K.-M. Weitzel, *J. Phys. Chem.* **107**, (2003) 10625.
39. W. G. Hwang, J. H. Moon, J. C. Choe, and M. S. Kim, *J. Phys. Chem. A* **102** (1998) 7512.
40. J. Troe, *J. Phys. Chem.* **87** (1983) 1800.
41. L. Brouwer, C. J. Cobos, J. Troe, H.-R. Dübal, and F. F. Crim, *J. Chem. Phys.* **86** (1987) 6171.
42. A. Fernandez, A. A. Viggiano, Th. M. Miller, S. Williams, and J. Troe, *J. Phys. Chem. A* **108** (2004) 9652.
43. A. I. Fernandez, A. A. Viggiano, A. I. Maergoiz, J. Troe, and V. G. Ushakov, *Int. J. Mass Spectrom.* **241** (2005) 305.
44. J. Troe, *Z. Phys. Chem.* **218** (2004) 1.
45. P. Botschwina, *ab initio* and DFT results, private communication (2004).